Enabling Flexible Heterostructures for Li-Ion Battery Anodes Based on Nanotube and Liquid-Phase Exfoliated 2D Gallium Chalcogenide Nanosheet Colloidal Solutions

Chuanfang John Zhang, Sang-Hoon Park, Oskar Ronan, Andrew Harvey, Andrés Seral-Ascaso, Zifeng Lin, Niall Mcevoy, Conor S. Boland, Nina C. Berner, Georg S. Duesberg, et al.

Enabling Flexible Heterostructures for Li-Ion Battery Anodes Based on Nanotube and Liquid-Phase Exfoliated 2D Gallium Chalcogenide Nanosheet Colloidal Solutions

Chuanfang (John) Zhang, Sang-Hoon Park, Oskar Ronan, Andrew Harvey, Andrés Seral-Ascaso, Zifeng Lin, Niall McEvoy, Conor S. Boland, Nina C. Berner, Georg S. Duesberg, Patrick Rozier, Jonathan N. Coleman,* and Valeria Nicolosi**

2D metal chalcogenide (MC) nanosheets (NS) have displayed high capacities as lithium-ion battery (LiB) anodes. Nevertheless, their complicated synthesis routes coupled with low electronic conductivity greatly limit them as promising LiB electrode material. Here, this work reports a facile single-walled carbon nanotube (SWCNT) percolating strategy for efficiently maximizing the electrochemical performances of gallium chalcogenide (GaX, X = S or Se). Multiscaled flexible GaX NS/SWCNT heterostructures with abundant voids for Li^+ diffusion are fabricated by embedding the liquid-exfoliated GaX NS matrix within a SWCNT-percolated network; the latter improves the electron transport and ion diffusion kinetics as well as maintains the mechanical flexibility. Consequently, high capacities (i.e., 838 mAh g^{-1} per gallium (II) sulfide (GaS) NS/SWCNT mass and 1107 mAh g^{-1} per GaS mass; the latter is close to the theoretical value) and good rate capabilities are achieved, which can be majorly attributed to the alloying processes of disordered Ga formed after the first irreversible GaX conversion reaction, as monitored by in situ X-ray diffraction. The presented approach, colloidal solution processing of SWCNT and liquid-exfoliated MC NS to produce flexible paper-based electrode, could be generalized for wearable energy storage devices with promising performances.

Dr. C. F. (John) Zhang, Dr. S.-H. Park, A. Harvey, Dr. A. Seral-Ascaso, Dr. N. McEvoy, Dr. C. S. Boland, Dr. N. C. Berner, Prof. G. S. Duesberg, Prof. J. N. Coleman, Prof. V. Nicolosi
Centre for Research on Adaptive Nanostructures and Nanodevices (CRANN) and Advanced Materials Bio-Engineering Research Centre (AMBER)
Trinity College Dublin
Dublin 2, Ireland
E-mail: zhangjc@tcd.ie; colemaj@tcd.ie; nicolov@tcd.ie

Dr. C. F. (John) Zhang, Dr. S.-H. Park, Dr. A. Seral-Ascaso, Dr. N. McEvoy, Dr. N. C. Berner, Prof. G. S. Duesberg, Prof. V. Nicolosi
School of Chemistry
Trinity College Dublin
Dublin 2, Ireland

O. Ronan, A. Harvey, Dr. A. Seral-Ascaso, Dr. C. S. Boland, Prof. J. N. Coleman
School of Physics
Trinity College Dublin
Dublin 2, Ireland

Dr. Z. Lin, Dr. P. Rozier
CIRIMAT
Université de Toulouse
CNRS, INPT, UPS, 118, route de Narbonne
31062 Toulouse Cedex 9, France

DOI: 10.1002/smll.201701677

1. Introduction

The incredible popularity of portable consumer electronics has greatly stimulated the development of safe, high-energy/power density, long cycle-life energy storage devices,[1–4] especially lithium-ion batteries (LiBs).[5] Commercial graphite anodes suffer from relatively low theoretical capacity (≈372 mAh g ^{1}) and sluggish ion kinetics (10 ^{11}–10^{-10} cm^{2} s ^{1})[6] upon Li^+ intercalation/de-intercalation.[7] Engineering the electrode by nanostructuring[8–10] or designing porous low-dimensional materials[11 14] may result in faster Li^+ diffusion and thus improve their rate capability.[15,17–20] Recently, 2D nanomaterials have attracted huge research attention for their use in LiBs due to their exotic properties.[21–23] As a typical example, the layered metal chalcogenides (MCs) including III–VI/IV–VI layered semiconductors (e.g., GaS, GaSe, InSe, and SnS_2) and transition metal dichalcogenides (e.g., MoS_2, WS_2, and ReS_2) possess higher specific capacities (>550 mAh g^{-1})[24,25] and larger interlayer spacing compared to graphite,[26–30] allowing a rapid Li^+ insertion/extraction process without inducing significant volume changes. Moreover, the weak van der Waals forces among the MC sheets facilitate the production of nanosheet (NS) dispersions via a facile exfoliation strategy.[31–33] To date, molybdenum disulfide (MoS_2) has been the most widely investigated layered MC for use as anodes in both LiB[34,35] and sodium-ion batteries.[36] Others, such as tungsten disulfide (WS_2)[5] and rhenium disulfide (ReS_2),[26,37] have recently been reported as having good electrochemical performances. Undoubtedly, the layered MC family is thus far relatively unexplored but shows remarkable potential for LiBs. Nevertheless, their poor electrical conductivity severely limits the electron transport and leads to a series of issues, such as low measured capacities, rapid capacity decay, and thus poor rate capability.[38,39] Incorporating the MC NS into a conductive scaffold such as graphene,[40] carbon nanotubes,[41] or conducting polymers,[42] for instance, could effectively maintain the structural integrity of the electrode while exposing more active sites to the electrolyte, resulting in much higher capacities as well as better rate capability.

As a representative member of layered MC family, gallium (II) sulfide (GaS) possesses an indirect bandgap of 2.5 eV and is of interest for many applications ranging from photoelectronics[43] to gas sensing.[44] However, a few studies have been conducted on GaS as an LiB anode material, apart from that of Meng et al., who deposited GaS_x thin films of quite low mass onto single-walled carbon nanotubes (SWCNTs) via atomic layer deposition, yielding a promising discharge capacity of 575 mAh g^{-1} (per total composite mass) and 770 mAh g^{-1} (per mass of GaS_x) at 120 mA g^{-1}.[24] However, this synthesis process is not scalable and can potentially give rise to the hazardous H_2S leakage in the temperature range used (150–200 °C). We believe for such materials to be competitive in LiB, a simple, scalable and environmentally friendly production of MC NS would be necessary.[30] To this end, liquid-phase exfoliation (LPE) has been widely recognized as an efficient, scalable and low-cost approach to obtain the 2D NS dispersions in suitable solvents.[33,45,46]

Herein, a facile SWCNT percolating strategy for efficiently maximizing the electrochemical performances of gallium chalcogenide (GaX. X = S or Se) is reported. Through environmentally friendly solution processing of SWCNT and liquid-phase exfoliated GaX NS, we obtained freestanding, flexible GaX NS/SWCNT heterostructures with NS matrix well embedded in the SWCNT-percolated network. Such a hierarchical nanostructure enables high capacities and fast rate capabilities in the GaX NS/SWCNT paper composite, holding great promise for practical LiB applications. The charge storage mechanism was studied by in situ X-ray diffraction. The superior electrochemical Li^+-storage performances could be ascribed to the advantages associated with the multiscaled hierarchical nanostructure at the same time: (i) the open channels might result in faster Li^+ diffusion. (ii) The entangled SWCNT network forms developed, percolated electron transport paths, lowering the junction resistance. (iii) SWCNT could function as a "conductive binder," maintaining the structural integrity of the thick electrode without losing electrical contact with the current collector.[47,48] Moreover, the absence of an insulating binder leads to dead-volume free electrode, allowing the composite to perform to its full potential. We believe the approach for the preparation of MC NS flexible conductive composites can be generalized, with the porous scaffold ranging from graphene to SWCNT, etc., while the NS could range from GaTe, InS, InSe, InTe, to other, yet untested, MC NS. The resultant composite films could find applications in wearable electronics and optoelectronics, energy-storage systems, or sensors, to name but a few.

2. Results and Discussion

In general, successful exfoliation of 2D materials is achieved when the energy cost of mixing with the solvent is minimized. This tends to occur for solvents with similar surface energy to the 2D material to be exfoliated.[33,45] In a previous report, we found that GaS could be well exfoliated in isopropanol (IPA);[33] therefore, in this work we similarly bath-sonicated the commercial GaS and GaSe powders,[49] utilizing the sonic energy to overcome the weak van der Waals coupling of the layers and forming an NS-enriched dispersion. This is schematically illustrated in **Figure 1**a. Scanning and transmission electron microscopy (SEM and TEM, respectively) of the obtained dispersions show large quantities of exfoliated NS with well-defined edges and no apparent damage in the basal planes, which confirms the good quality of the exfoliated material (Figure 1b-e).[50] Statistical analysis of the TEM images determines that the GaS NS have $\langle L \rangle = 413 \pm 26$ nm (the inset of Figure 1c), in good agreement with $\langle L \rangle = 410$ nm derived from the measured extinction and absorption spectra, as well as the subtracted scattering spectra (Figure 1f).[50,51] Using previously determined metrics from the extinction spectra the GaS NS concentration is found to be 2 mg mL^{-1}.[50,51]

As for the GaSe, the as-prepared solution exhibits an orange color (the inset of Figure 1d). The TEM in Figure 1d indicates the curved morphology of the GaSe NS with mean

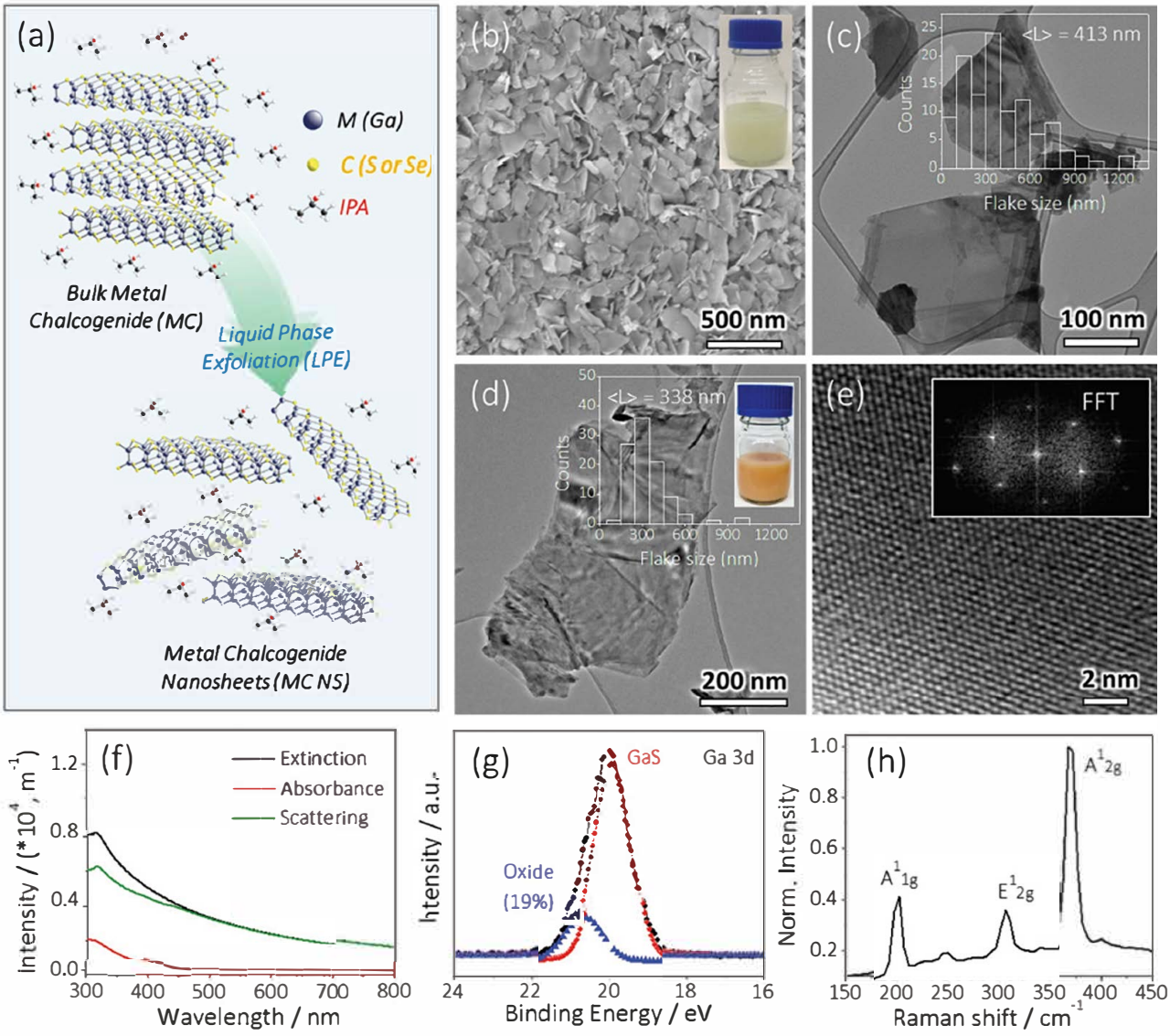

Figure 1. a) Schematic of MC NS production through a liquid-phase exfoliation approach. b) SEM and c) TEM of exfoliated GaS NS. Inset in part (c) is the GaS NS size distribution. d) TEM and e) high-resolution TEM of exfoliated GaSe NS. Insets in parts (d) and (e) are the size distribution and fast Fourier transform pattern of exfoliated GaSe NS, respectively, showing a highly crystalline structure. f) Optical extinction, absorbance, and scattering spectra of a typical GaS NS dispersion. Here, intensity represents Extinction, Absorbance, or Scattering as appropriate. g) Ga 3d XPS and h) Raman spectrum of exfoliated GaS NS.

flake size of 338 ± 38 nm (Figure 1d and its inset). The high-resolution TEM and its corresponding fast Fourier transform pattern are shown in Figure 1e and its inset, respectively, showing the highly crystalline structure of the exfoliated GaSe NS.

To investigate if defects were introduced to the GaS NS during sonication, both X-ray photoelectron spectroscopy (XPS) and Raman spectroscopy were performed. The deconvoluted XPS of the Ga 3d core level (Figure 1g) shows that the GaS NS exhibits only a small amount of degradation from a Ga_xO_y component which can be found at a slightly higher binding energy than the dominant GaS species. The characteristic lattice vibrations at 195, 301, and 370 cm^{-1} corresponding to the GaS A^1_{1g}, E^1_{2g}, and the A^1_{2g} modes, respectively, are found in the Raman spectrum displayed in Figure 1h.[43,52]

Next, binder-free flexible composite electrodes were prepared, assisted by a vacuum filtration of the mixture of MC NS/SWCNT dispersions, as shown in **Figure 2**a. As references, pure MC NS and SWCNT films were similarly produced. A typical TEM image of SWCNT is shown in Figure S1 (Supporting Information). According to previous reports, the mass fraction of the conductive agent is of critical importance to the electrical conductivity and mechanical properties (flexibility) of the NS/SWCNT and NS/graphene composites.[41,53] Therefore, the effect of SWCNT mass fraction on both properties of the GaS NS/SWCNT composites is explored. In the case of the MC NS only film, the electrical conductivity was too low to measure. The 5% SWCNT composite exhibits 0.2 S m^{-1} but dramatically increases up to 1491 S m^{-1} for 50% SWCNT, as shown in Figure 2b. Such an increase in electrical conductivity is usually interpreted via percolation theory.[54]

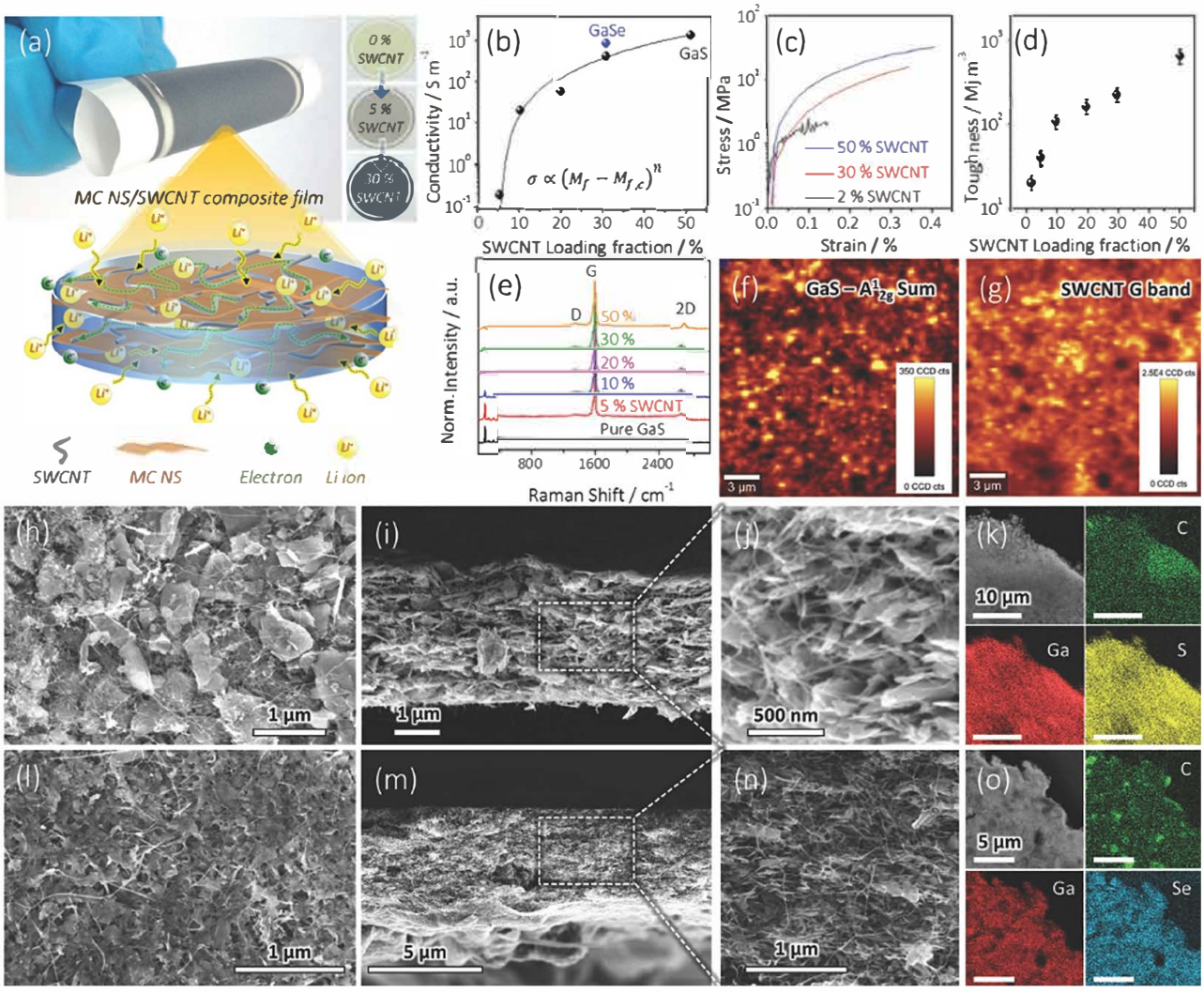

Figure 2. a) Schematic describing the critical role of SWCNT in constructing a multiscaled hierarchical nanostructure. Insets are the GaS NS-based thin films with 0%, 5%, and 30% SWCNT. b) Electrical conductivity of GaS and GaSe NS-based composites with different SWCNT-loading fractions. The fitted line was obtained *via* percolation theory. c) Representative stress–strain curves and d) tensile toughness plotted as a function of SWCNT-loading fraction in GaS NS/SWCNT composite films. e) Raman spectra of GaS NS/SWCNT composites. Scanning Raman spectroscopy of f) GaS A^1_{2g} and g) SWCNT G band. h) SEM and i,j) cross-sectional SEM images of GaS NS/SWCNT composite (30% SWCNT, 5 µm) at i) low and j) high magnification. k) EDX mapping of Ga, S, and C in GaS NS/SWCNT composite. Scale bar is 10 µm. l) SEM and m,n) cross-sectional SEM images of GaSe NS/SWCNT composite (30% SWCNT, 5 µm) at m) low and n) high magnification. o) EDX mapping of Ga, Se, and C in GaSe NS/SWCNT composite. Scale bar is 5 µm.

The measured conductivity was further analyzed using the following equation:

$$\sigma \propto (M_f - M_{f,c})^n \quad (1)$$

where σ is the conductivity, M_f is the SWCNT mass loading fraction, $M_{f,c}$ is the threshold of SWCNT fraction to form the first conductive paths, and n is the exponent.[54] While percolation analysis is usually performed on data plotted versus filler volume fraction, it can easily be shown that, in porous films, the mass and volume fractions are directly proportional, making the analysis below appropriate. The good fit of this model to the data shown in Figure 2b suggests that the addition of SWCNT follows percolation theory.[47] From the fitted results an $n = 2.5$ is found, similar to the universal percolation exponent ($n = 2.0$) and very close to the value of 2.3 obtained by Liu et al. for MoS_2/SWCNT composites.[41] Although we were not able to measure the conductivity for samples below 5% SWCNT, the data are consistent with a percolation threshold of ≈3.5%, somewhat larger than the value of ≈1 % reported by Liu et al.

In addtion to the electrical percolation, the SWCNT loading fraction also determines the mechanical properties of such composites.[41] As illustrated in Figure 2c, upon increasing SWCNT content from 2% to 50%, both the strain and stress performances are dramatically improved. Furthermore, the toughness (energy density absorbed at fracture) as a function of SWCNT mass fraction (Figure 2d) was plotted, showing a drastic improvement in the toughness as the SWCNT fraction is initially increased up to 10%. We would

expect such a toughness increase to help the composite survive the expansion/contraction cycles associated with repeated charging/discharging.[41]

Raman spectra of the GaS NS/SWCNT composite films show the characteristic peaks of GaS (Figure 2e) as well as peaks from SWCNT (≈1340 cm^{-1}, ≈1580 cm^{-1}, and ≈2675 cm^{-1}, indexed as the characteristic D, G and 2D bands, respectively).[55] A plot of relative GaS Raman intensity versus SWCNT loading fraction is shown in Figure S2 (Supporting Information). At high SWCNT fraction, the contribution from radial breathing modes of SWCNT[56] is seen in the low-frequency regime, partially overlapping with the GaS A_{1g} mode (Figure S2a, Supporting Information). A color-coded map, showing contributions from both SWCNTs and GaS, is presented in Figure S2b (Supporting Information). On the basis of the normalized Raman intensity, the I_{GaS}/I_{SWCNT} as a function of the electrode composition $(1/M_L - 1)$ was plotted, revealing a good linear fit (Figure S2c, Supporting Information). It is worth mentioning that, since the 30% SWCNT composite possesses good conductivity (Figure 2b), mechanical toughness (Figure 2c,d) and uniformity, as seen from the homogeneous distribution of SWCNT and GaS signals over the entire mapped area in its scanning Raman spectroscopy (Figure 2f,g), we selected 30% as the optimized SWCNT loading fraction in the GaS/GaSe NS/SWCNT composite films.

Figure 2h is an SEM image of the GaS NS/30% SWCNT, showing that the GaS NS are uniformly embedded in the SWCNT network. The cross-sectional SEM image of the GaS NS/30% SWCNT composite shown in Figure 2i displays a thickness of ≈4–5 μm, consistent with the thickness obtained with a digital micrometer. The enlarged SEM image shows that the GaS NS is uniformly spread within the SWCNT network (Figure 2j), which creates sufficient void space for rapid Li^+ diffusion as well as volume expansion and also prevents the GaS NS from aggregating. The homogeneous distribution of both nanotubes and nanosheets within the composite was confirmed by elemental mapping of Ga, S, and C performed by energy-dispersive X-ray spectroscopy (EDX) in the SEM (Figure 2k).

As for the GaSe NS/30% SWCNT composite, it exhibits a slightly higher electrical conductivity of 954 S m^{-1} (Figure 2b). The exfoliated GaSe NS are well embedded in the SWCNT percolated network (Figure 2l–n), forming a homogeneous composite. The EDX mapping of Ga/Se/C elements in Figure 2o also indicates a uniform composition across the electrode. For the sake of simplicity, we term the MC NS/30% (5 μm) SWCNT composites as GaS NS/SWCNT and GaSe NS/SWCNT for the further studies unless specifically noted.

The electrochemical performance of the GaS NS/SWCNT composite was investigated through cyclic voltammetry (CV) and galvanostatic charge/discharge (GCD), and compared to that of GaS NS. **Figure 3**a shows CV curves at a scan rate of 0.2 mV s^{-1}. The sharp cathodic peak starts at 1.1 V in the first cycle, then gradually weakens in the following cycles, and eventually disappears in the tenth cycle, suggesting that the composite film possibly undergoes structural change, which could be expressed by the following conversion reactions:[25]

$$GaS + 2Li^+ + 2e^- \rightarrow Ga + Li_2S \quad (2)$$

as well as the formation of solid electrolyte interphase (SEI).[57] This process is similar to the conversion reaction of MoS_2/SWCNT anode.[41] The obvious plateau at 1.0–1.1 V in the first discharge profile (Figure S3a, Supporting Information) agrees well with the CV result. The cathodic peaks centered at 0.6 and 0.1 V could be attributed to the formation of LiGa and Li_2Ga alloy phases, respectively, according to the following overall reaction:[58,59]

$$Ga + 2Li^+ + 2e^- \leftrightarrow Li_2Ga \quad (3)$$

Upon anodic scanning, peaks centered at 0.5 V and 0.8 V, are found, corresponding to de-alloying of Li_2Ga and LiGa phases to Ga, respectively.[58,59] The absence of sharp peaks in anodic scanning should indicate that the conversion mechanism of GaS (reaction (2)) is irreversible. Based on the above reactions, a theoretical capacity of around 1053 mAh g^{-1} for GaS (assuming four electrons transfer during the lithiation) was obtained. Although the initial discharge capacities of the two materials are similar (1730 mAh g^{-1}, Figure S3a, Supporting Information), the composite retains a much higher discharge capacity (838 mAh g^{-1}) than that of pure GaS NS (576 mAh g^{-1}) after five cycles at 100 mA g^{-1} (Figure 3b). Close examination reveals that broad CV curves (Figure 3a) as well as sloping GCD profiles (Figure S4a, Supporting Information) are found in the composite film, in contrast to the sharp CV peaks and discharge plateau in the GaS NS (**Figure 4**b). This implies that the charge-storage mechanism has changed from traditional battery type to pseudocapacitive type upon the introduction of SWCNT.[60] Such a critical adjustment, we believe, is important, as charge could be injected/ejected much faster in the case of pseudocapacitive behavior.[15,61,62] As indicated in Figure 2a, the randomly distributed SWCNT could simultaneously serve both as the conductive "spacer" and "binder" between the GaS NS, forming a multiscaled hierarchical nanostructure with many surface Li^+ storage sites and shortened ion diffusion paths, which could be responsible for the broad CV and sloping GCD curves in the composite films. In the absence of SWCNT, the GaS NS easily restack to form the multilayered GaS bulk phase (as shown in Figure 1b) and thus decrease the surface Li^+ storage sites, leading to apparent lower capacity values and fast capacity decay. Actually, the fact that the MC-based conductive composite exhibits a pseudocapacitive charge storage mechanism is not unexpected. Very recently, Dunn and co-workers studied a TiS_2 composite electrode, which demonstrated pseudocapacitive intercalated behavior in its 2D nanoscaled morphology that is not exhibited in the corresponding bulk TiS_2.[63] Another study by Park and co-workers also shows that the electrochemical behavior of MoS_2 could change from the dominated sluggish diffusion control to pseudocapacitive provided the layered MoS_2 was scaled down into nanometric sheets and percolated with a reduced graphene oxide network.[64]

To further understand the charge storage mechanisms, in situ X-ray diffraction (XRD) of the GaS NS/SWCNT composite electrode was performed, and the patterns were

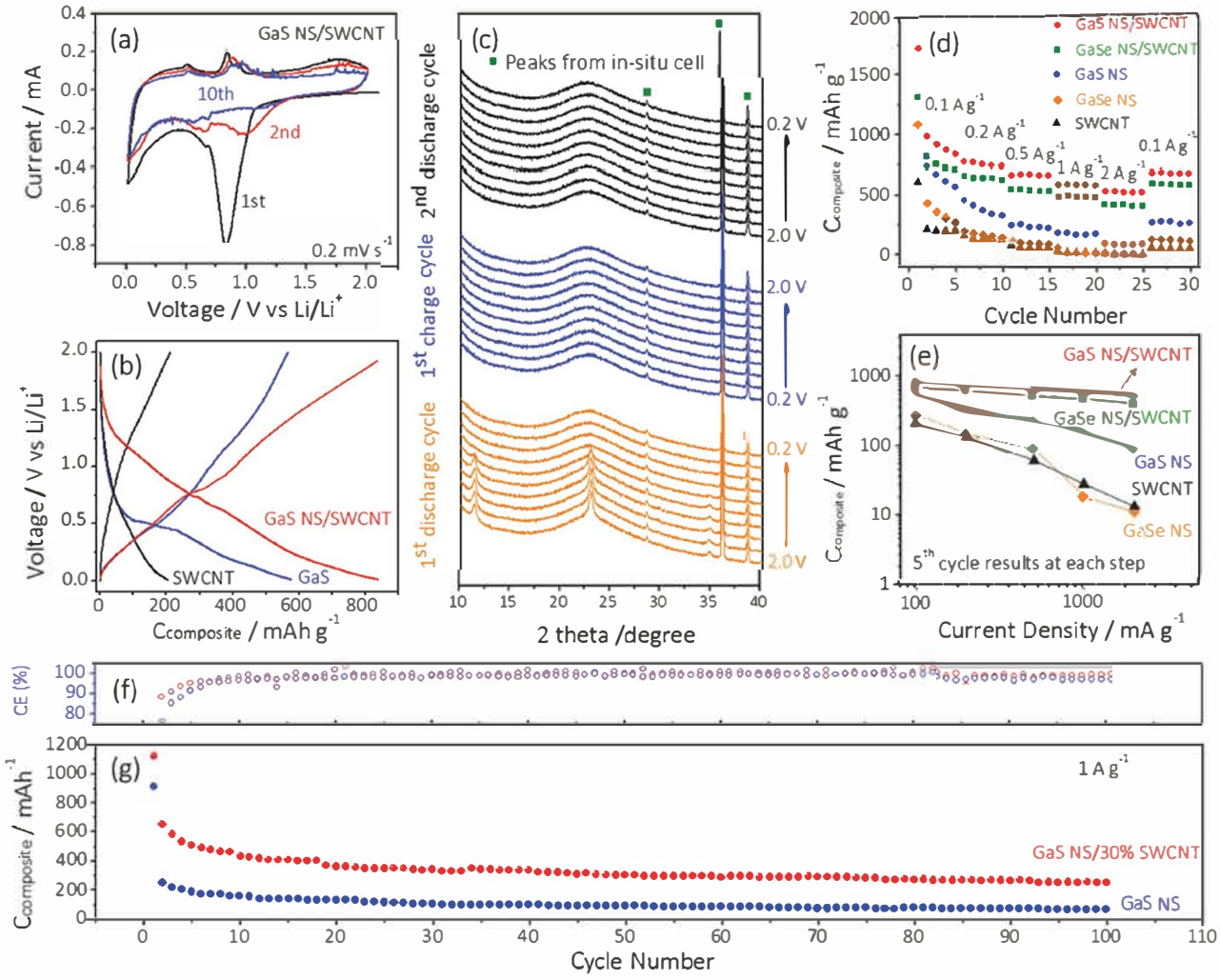

Figure 3. a) Cyclic voltammograms of GaS NS/SWCNT composite (30% SWCNT, 5 μm) at a scan rate of 0.2 mV s^{-1}. b) Fifth galvanostatic charge/discharge profiles of SWCNT, GaS NS, and GaS NS/SWCNT composites (30% SWCNT, 5 μm) at a current density of 100 mA g^{-1}. c) In situ XRD patterns of GaS NS/SWCNT composites at different potentials with a fix step of 0.2 V versus Li/Li^+. d) Rate performance of SWCNT, GaS, and GaSe NS-based samples at different current densities ranging from 100 mA g^{-1} to 2 A g^{-1}; all the samples have very similar thickness (5 μm). e) Specific capacities as a function of current density; here, the capacity at the fifth cycle under each current was selected. f) Coulombic efficiency and g) cycling performance of GaS NS and GaS NS/SWCNT composite at 1 A g^{-1}.

recorded at various potentials with a fix potential step of 0.2 V as seen in Figure 3c. Peaks centered at 28°, 36°, and 38° come from the in situ cell setup. Beside the broad signal around 23°, corresponding to the SWCNT scaffold, three other peaks at, respectively, 11°, 23°, and 34° are found at open circuit potential (2.0 V), corresponding to (002), (004), (006) planes of GaS. The evidence of these (00l) peaks suggests the periodic stacking of the GaS NS. The (00l) peaks are maintained down to 1.2 V, then start to weaken at 1.0 V and eventually disappear below 0.8 V, indicating the disordering of the structure induced by the lithiation of the GaS during the discharge process, which is irreversible, as no (00l) peaks are recovered upon the following charge cycle. Said otherwise, there is no evidence for the growing of crystalline GaS in agreement with the irreversible conversion of GaS (reaction (2)) deduced from the CV, the capacity is majorly contributed by the Ga alloy process according to reaction (3). However, the absence of the Ga and Li_xGa characteristic peaks suggests that either the crystal growth of these two species is suppressed, or they are small and disordered.[59]

The rate performances are shown in Figure 3d. Compared to pure GaS NS, the GaS NS/SWCNT composite displays much better capacity and rate capability (Figure 3e). For example, at 2 A g^{-1}, the specific capacity of the GaS NS/SWCNT composite is 530 mAh g^{-1}, almost six times higher than that of pure GaS NS (92 mAh g^{-1}). When the current is switched back to 100 mA g^{-1} after 25 cycles, the capacity returns to 700 mAh g^{-1}. GCD profiles of two electrodes at various current densities could be seen in Figure S4a,b (Supporting Information). We believe the rapid capacity decay of GaS NS could be attributed to the absence of SWCNT, which provides the efficient conductive network and maintains the structural integrity. Moreover, the composite's capacity greatly exceeds that of GaS NS and SWCNT when the current density is beyond 200 mA g^{-1}, indicating that the synergistic effect between the two components has

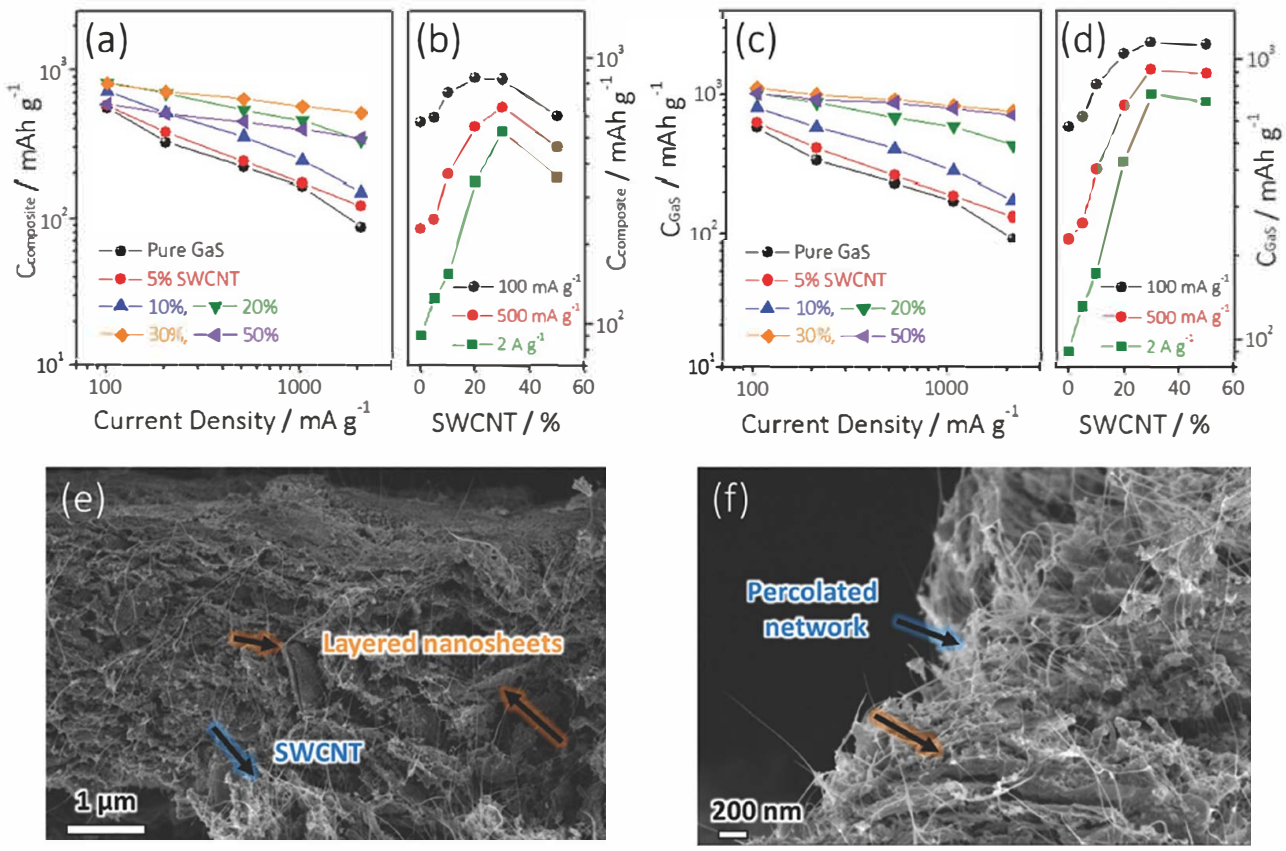

Figure 4. Specific capacities of GaS NS/SWCNT composites as a function of a) current density and b) SWCNT-loading fractions. Here, the capacity at the fifth cycle under each current was selected. Utilization of GaS NS calculated based on Equation (4) as a function of c) current density and d) SWCNT loading fraction. SEM images of cycled GaS NS/SWCNT electrode after 100 cycles at e) low and f) high magnification.

been the reason for the superior Li^+ storage performances. The cycling performances of GaS NS and GaS NS/SWCNT are evaluated at a high rate (1 A g^{-1}), as shown in Figure 3f,g. GaS NS exhibits a low first cycle Coulombic efficiency (iCE, 19%; Figure 3f) and a poor lifetime performance (only 77 mAh g^{-1} is retained after 100 cycles, Figure 3g). After embedding the GaS NS in the SWCNT scaffold, both the first cycle CE and the capacity retention have been improved considerably (iCE = 60% and retains 300 mAh g^{-1}, Figure 3g). The improved iCE should be ascribed to the enhanced electrical conductivity and mechanical property brought by the SWCNT-percolated network. Further increasing of iCE could be realized by adding less SWCNT with higher conductivity but lower surface area. As such, the irreversible capacity loss from SEI formation is minimized. Although the iCE of the composite is moderate, it is much higher than the graphene/SWCNT/nickel composite anode material (iCE = 30%).[65] The rapid capacity decay in the first ten cycles could be attributed to the irreversible GaS conversion, as seen in Figure 3a,c. The gradual capacity decay phenomenon is commonly observed in conversion/alloy-type electrodes and has been attributed to the incomplete conversion, pulverization, and loss of electrical contact with the SWCNT upon cycling.[13,57] Moreover, the dissolution and shuttling of intermediate Li_2S could be responsible for the capacity fading, similar to the cycling issues that exist in Li–sulfur batteries. Since this is an early-stage report on the GaS NS/SWCNT composite, there is certainly much scope to improve the cycle life by gaining increased understanding of its electrochemical process, i.e., ensuring intimate contact between the active GaS and the SWCNT scaffold, facilitating more complete conversion and alloying processes, etc.

GCD curves of GaSe NS and GaSe NS/SWCNT are shown in Figures S3c and S4c,d (Supporting Information), revealing first discharge capacities of 1090 and 1320 mAh g^{-1}, respectively. A more sloping curve is found in the composite in sharp contrast to plateaus seen for the GaSe NS at all current densities, further confirming that the addition of SWCNT is beneficial for increasing the Li^+ storage sites, shortening ion diffusion paths and resulting in a pseudocapacitive behavior. The rate performances of GaSe NS and GaSe NS/SWCNT are summarized in Figure 3d,e. The composite shows a discharge capacity of 713 mAh g^{-1} at 100 mA g^{-1} and 413 mAh g^{-1} at 2 A g^{-1}, slightly lower capacity values but similar rate capabilities compared to the GaS NS/SWCNT counterpart. Therefore, GaS NS was selected for fabricating MC NS/SWCNT films with different compositions and thickness. The capacities normalized to the total mass of the electrodes are plotted as a function of current density and SWCNT loading fraction as seen in Figure 4a,b. The rate performance of the composites can be found in Figure S5 (Supporting Information). Both the capacities and the rate performances are remarkably improved upon increasing the SWCNT loading fractions from 5% to 30%, consistent with the improvement

in electrical conductivity as well as mechanical properties demonstrated by Figure 2b-d. However, excessive SWCNT (50%) addition results in a smaller portion of redox-active GaS NS in the composite and thus decreases the capacity substantially, as seen in Figure 4a,b. While it is of more practical importance to investigate the specific capacities normalized to the total composite mass, it is also fundamentally valuable to understand the utilization of the GaS NS, more precisely how their inherent capacity contributes to the total capacity of the composite electrode. The utilization of GaS NS in each composite was quantitatively determined according to Equation (4):

$$C_{GaS} = \left(C_{composite} - C_{SWCNT} \times \%_{SWCNT}\right) / \%_{GaS} \quad (4)$$

Where C_{GaS}, $C_{composite}$, and C_{SWCNT} represent, respectively, the specific capacity per GaS NS, composite, and SWCNT, while $\%_{SWCNT}$ and $\%_{GaS}$ are the mass loading fractions of the SWCNT and GaS NS, respectively. Here, the C_{SWCNT} in each composite is supposed to be the same as that of Figure 3d. Figure 4c plots the utilization of GaS NS in various composites as a function of current density. When increasing the $\%_{SWCNT}$ from 5% to 50%, the C_{GaS} increases dramatically at first and then saturates (Figure 4d), suggesting that 30% SWCNT seems to allow the GaS NS to reach its intrinsic capacity values, as shown by the plateau. If so, then the corresponding capacity at the plateau should match the theoretical value based on Equations (2) and (3). Encouragingly, the C_{GaS} at 100 mA g^{-1} agrees well with the theoretical capacity (1107 vs 1053 mAh g^{-1}, respectively). As for the GaSe NS, its utilization reaches 928 mAh g^{-1} in the composite at 100 mA g^{-1}. Such a remarkably high capacity per MC NS component greatly exceeds that of the atomic-layer-deposited GaS_x–SWCNT composite (766 mAh g^{-1}).[24] The electrochemical impedance spectroscopy (EIS) in Figure S6 (Supporting Information) also suggests that by gradually adding SWCNT up to 30%, the semicircle at high/medium-frequency region decreases, implying a smaller charge-transfer resistance (R_{ct}) and easier semidiffusion process of Li^+ into the GaS NS host. The effect of mass loading on the areal capacity of GaS NS/SWCNT composite is analyzed in detail in Figures S7–S10 (Supporting Information). After cycling, the GaS NS/SWCNT composite still preserves its 2D layered morphology, demonstrating the percolated network maintains the structural integrity upon repeated charging/discharging (Figure 4e,f).

Figure 5 compares the electrochemical performances of MC-containing electrode systems in detail (note that Table S1 (Supporting Information) provides details and references). It should be specially noted that, in order to eliminate the effect of the materials' morphology on the capacities, only materials with a 2D layered structure, such as nanosheets, nanoflakes, or nanoplatelets, were chosen from the large MC family. We emphasize that it is rather challenging to make a direct comparison among various systems due to a large number of variables, such as mass loading/film thickness, potential range, binder/conductive additive fractions, and nanosheet size. Taking this into account as much as possible, firstly the literature-specified capacities were normalized based on the mass of active MC and total electrode, and then categorized the values according to the mass loading as well as the potential

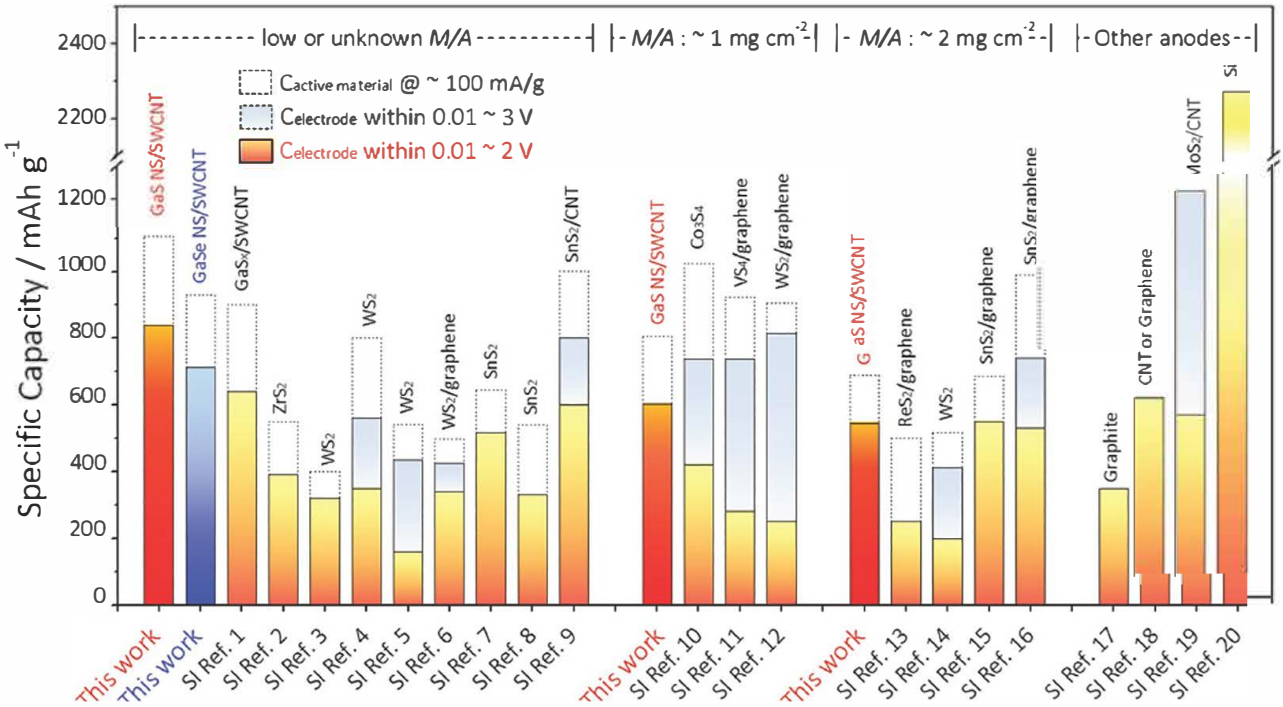

Figure 5. Comparison of the specific capacities of this work to various 2D MC-containing electrode systems when normalized to the mass of active MC as well as the total electrode material. Values are classified according to the mass loading and potential range. Table S1 (Supporting Information) provides details and references. For the purpose of comparison, we also include graphite, CNT/graphene and Si-based anodes.

range. It is worth mentioning that an anode with lower potential is more desirable for achieving a higher energy/power density in LiBs. Unlike the half-cell configuration that emphasizes the discharge capacity regardless of the electrode being anode or cathode, a full-cell battery system relies on the charge capacity of the anode. Therefore, for those systems tested in the 0.01–3 V window, the charge capacities that were achieved in the range 0.01–2 V were extracted to facilitate our comparison. The compiled plot shows that our binder-free GaS NS/SWCNT and GaSe NS/SWCNT flexible composites perform much better than any other 2D MC-based electrode systems in terms of capacity per active MC and per electrode in the 0.01–2 V window. For example, the utilization of GaS NS reached remarkably high (1107 mAh g^{-1}). In addition, our composite film outperforms most other electrode systems in the high-mass loading region (2 mg cm^{-2}), except for the SnS_2/graphene anode by Zhao et al., who tested the composite at a lower current density.[16] This clearly indicates the advantages of the flexible, binder-free composites and highlights its state-of-the-art performance.

3. Conclusion

In summary, the facile, environmentally friendly production of multiscaled hierarchical GaX NS/SWCNT heterostructures is demonstrated. Through a colloidal solution processing approach, the NS matrix embeds well within the SWCNT percolated network, enabling excellent rate capability and high specific capacity (838 mAh g^{-1} in GaS NS and 713 mAh g^{-1} in GaSe NS) as the LiB anode material. Moreover, due to the efficient Li^+ diffusion and electron transport kinetics, the composite film exhibits remarkably high utilization of GaX NS (1107 mAh g^{-1} in GaS NS and 928 mAh g^{-1} in GaSe NS), demonstrating electrochemical performances competitive with those of other reported 2D MC-based electrode systems. This work opens up vast opportunities for other families of MC NS to be scalably processed into flexible conductive composite films with a broad range of applications such as wearable electronics and optoelectronics, energy storage systems, sensors, and fuel cells.

4. Experimental Section

Exfoliation of MC NS and Preparation of SWCNT Dispersion: GaS NS were obtained through LPE of commercial GaS powder (99.999% GaS-05-P, American Elements) using an ultrasonic bath (P30 H Ultrasonic from Fischer scientific) in IPA.[50] First, the GaS powder was added into 20 mL of IPA at a concentration of 45 mg mL^{-1}, then the suspension was sonicated for 6 h at an amplitude of 100% and a frequency of 37 kHz. During sonication, the temperature of the bath was cooled to 20–30 °C by continuous flow of cooling water. Once sonicated, the dispersion was subjected to centrifugation (Hettich Mikro 220R) for 180 min at 1000 rpm. The top 60% supernatant was collected while the sediment was recycled to produce an adequate quantity of GaS NS. SWCNT (P3-CNT, Carbon Solutions, Inc.) was dispersed in IPA at a concentration of 0.1 mg mL^{-1} using bath sonication. GaSe NS was similarly prepared by sonication the commercial GaSe powders in IPA.

Flexible MC NS/SWCNT Composite: The composites were prepared through a facile vacuum filtration approach of blended dispersion though a polyethylene membrane (Celgard K2045, 0.06 μm pore size). Several GaS NS/SWCNT composite films were prepared with SWCNT contents being 5%, 10%, 20%, 30%, and 50%, respectively, while keeping the filtrated volume constant (20 mL). Composites with different thickness were also prepared by controlling the filtrated volume to 20, 40, 80, and 160 mL, respectively. To avoid degradation over time, the films (including the membrane) were immediately transferred to a glove box (oxygen and water content <1 ppm). The natural dried films were then cut into individual electrodes with 7 mm × 7 mm size (geometric area ≈0.5 cm^2). It is worth noting that the attached membrane was utilized as a second separator in the coin cells. This was clearly different from many reported freestanding electrodes, which were obtained through complicated peeling off or film transfer procedures.[39,66] For the GaSe NS/SWCNT composite, the SWCNT loading fraction was controlled at 30%.

Materials Characterization: The SEM images were obtained on a Zeiss Ultra Plus (Carl Zeiss, Germany) working at 2 keV of acceleration voltage. EDX was performed in the same microscope and analyzed using INCA program. TEM analysis of the MC NS and SWCNT was performed on an FEI Titan at 300 kV (FEI, USA). The nanosheet dispersion was drop-casted onto holey carbon grids (Agar Scientific, UK). The flake dimensions were statistically analyzed on TEM by measuring the longest axis of the nanosheets and assigning it as the length. Optical spectroscopy was done on GaS NS dispersion using an UV–vis absorbance spectroscopy (Cary 6000i Spectrometer, Agilent, USA). Both the extinction and absorption spectra of the dispersion were measured using an integrating sphere that subtracted the absorption spectra from the extinction spectra. To show the quality and defects of the as-exfoliated GaS NS, X-ray photoelectron spectroscopy and Raman spectroscopy were conducted. XPS was performed using monochromated Al Kα X-rays from an Omicron XM1000 MkII X-ray source with an EA125 energy analyzer, which yielded a maximum energy resolution of ≈0.65 eV. All the binding energy scale was referenced to the aliphatic carbon 1s core-level at 284.8 eV. Raman spectra of GaS NS were acquired using a WITec Alpha 300 R with a 532 nm excitation laser at a power of ≈150 μW. A 100× objective was used with a spectral grating of 600 lines mm^{-1}. Characteristic spectra were obtained by averaging 20 discrete point spectra for each sample. For the composite electrodes, Raman maps were obtained by acquiring 80 × 80 spectra over an area of 20 × 20 μm. Maps representing the presence of SWCNT were generated by mapping the intensity of the SWCNT G band whereas the presence of GaS was represented by the intensity of the GaS A^1_{2g} band. The DC electrical conductivity of the composites was measured using a two-point probe technique. Two parallel electrode contacts were created on the film surface using conductive silver paint (Agar Scientific). The resistance of each sample was measured using a Keithley 2400 source meter. The electrode thickness was determined by a digital micrometer (Mitutoyo). In order to perform mechanical measurements, the GaS NS/SWCNT was peeled off composites (with different SWCNT loading fractions) after vacuum filtration. The free-standing films were then cut into stripes, 2.25 mm wide. The mechanical measurements were conducted on the Zwick tensile tester using a

gauge length of 5 mm and a strain rate of 1 mm min^{-1}. Each data point was an average of four measurements.

Electrochemical Characterization: The electrochemical performances of the GaS and GaSe NS/SWCNT flexible composites were investigated using CR-2032 coin cells. Two layers of polypropylene membrane (K2045 Coated PP, Celgard LLC, Charlotte, NC) were used as a separator. The composite electrode (attached on the PP) was used as the working electrode while a lithium metal disc with a diameter of 16 mm was used as both the counter and reference electrodes. The electrolyte was 1 M lithium perchlorate ($LiClO_4$) dissolved in ethylene carbonate and dimethyl carbonate in a volume ratio 1:1. Electrochemical tests were performed through CV, GCD, and EIS with a voltage range of 0.05–2 V on a potentiostat (VMP3, Biologic). In the CV, electrodes were cycled for ten times at 0.2 mV s^{-1}. For GCD, tests were conducted with current densities ranging from 100 to 2000 mA g^{-1}. The capacities reported here were those obtained from the sixth discharge profile at each current density and normalized to either the mass of active material (GaS NS) or the total mass of composite (GaS NS/SWCNT). The cycling performance of the electrodes was evaluated at 1000 mA g^{-1} for 100 cycles. The EIS was conducted at the open-circuit potential with the AC frequencies ranging from 200 kHz to 10 mHz.

Supporting Information

Supporting Information is available from the Wiley Online Library or from the author.

Acknowledgements

C.F.Z. and S.-H.P. contributed equally to this work. V.N., C.F.Z., S.-H.P., A.S.-A., O.R. wish to acknowledge the following funding support: SFI AMBER, SFI PIYRA, ERC StG 2DNanoCaps, ERC PoC 2DUSD, ERC PoC 2DInk, FP7 MC ITN MoWSeS, Horizon2020 NMP Co-Pilot. J.N.C. acknowledges the ERC SEMANTICS and SFI (11/PI/1087) for financial support. N.M. was supported by the SFI under 15/SIRG/3329, and N.C.B. and G.S.D. acknowledge SFI PI_10/IN.1/I3030. Z.L. was supported by China Scholarship Council (Grant No. 201304490006). All authors wish to thanks the Advanced Microscopy Laboratory (AML) in CRANN, Trinity College. S. O'Brien and A. Pokle are also acknowledged and thanked for the help provided. S. O'Brien, A. Pokle, and J. Coelho are appreciated for the experimental help.

Conflict of Interest

The authors declare no conflict of interest.

[1] P. G. Bruce, B. Scrosati, J.-M. Tarascon, *Angew. Chem. Int. Ed.* **2008**, *47*, 2930.
[2] J. B. Goodenough, Y. Kim, *Chem. Mater.* **2010**, *22*, 587.
[3] C. Zhang, T. M. Higgins, S.-H. Park, S. E. O'Brien, D. Long, J. N. Coleman, V. Nicolosi, *Nano Energy* **2016**, *28*, 495.
[4] C. Zhang, K. B. Hatzell, M. Boota, B. Dyatkin, M. Beidaghi, D. Long, W. Qiao, E. C. Kumbur, Y. Gogotsi, *Carbon* **2014**, *77*, 155.
[5] R. Chen, T. Zhao, W. Wu, F. Wu, L. Li, J. Qian, R. Xu, H. Wu, H. M. Albishri, A. S. Al-Bogami, D. A. El-Hady, J. Lu, K. Amine, *Nano Lett.* **2014**, *14*, 5899.
[6] P. Yu, *J. Electrochem. Soc.* **1999**, *146*, 8.
[7] C. Zhang, Y. Xie, G. Sun, A. Pentecost, J. Wang, W. Qiao, L. Ling, D. Long, Y. Gogotsi, *J. Electrochem. Soc.* **2014**, *161*, 1486.
[8] L. Ji, Z. Lin, M. Alcoutlabi, X. Zhang, *Energy Environ. Sci.* **2011**, *4*, 2682.
[9] Y.-G. Guo, Y.-S. Hu, W. Sigle, J. Maier, *Adv. Mater.* **2007**, *19*, 2087.
[10] L. He, C. Wang, X. Yao, R. Ma, H. Wang, P. Chen, K. Zhang, *Carbon* **2014**, *75*, 345.
[11] Y. Wu, H. Wu, S. Luo, K. Wang, F. Zhao, Y. Wei, P. Liu, K. Jiang, J. Wang, S. Fan, *RSC Adv.* **2014**, *4*, 20010.
[12] Y. Sun, S.-B. Yang, L.-P. Lv, I. Lieberwirth, L.-C. Zhang, C.-X. Ding, C.-H. Chen, *J. Power Sources* **2013**, *241*, 168.
[13] J. Chang, X. Huang, G. Zhou, S. Cui, P. B. Hallac, J. Jiang, P. T. Hurley, J. Chen, *Adv. Mater.* **2013**, *26*, 758.
[14] F. Du, H. Tang, L. Pan, T. Zhang, H. Lu, J. Xiong, J. Yang, C. Zhang, *Electrochim. Acta* **2017**, *235*, 690.
[15] C. Zhang, R. Maloney, M. R. Lukatskaya, M. Beidaghi, B. Dyatkin, E. Perre, D. Long, W. Qiao, B. Dunn, Y. Gogotsi, *J. Power Sources* **2015**, *274*, 121.
[16] S. Y. Liu, X. Lu, J. Xie, G. S. Cao, T. J. Zhu, X. B. Zhao, *ACS Appl. Mater. Inter.* **2013**, *5*, 1588.
[17] L. Kong, C. Zhang, J. Wang, W. Qiao, L. Ling, D. Long, *Sci. Rep.* **2016**, *6*, 21177.
[18] Y. Wei, Y. Tao, C. Zhang, J. Wang, W. Qiao, L. Ling, D. Long, *Electrochim. Acta* **2016**, *188*, 385.
[19] L. Kong, C. Zhang, J. Wang, D. Long, W. Qiao, L. Ling, *Mater. Chem. Phys.* **2015**, *149–150*, 495.
[20] C. Zhang, M. Beidaghi, M. Naguib, M. R. Lukatskaya, M.-Q. Zhao, B. Dyatkin, K. M. Cook, S. J. Kim, B. Eng, X. Xiao, D. Long, W. Qiao, B. Dunn, Y. Gogotsi, *Chem. Mater.* **2016**, *28*, 3937.
[21] M. Chhowalla, Z. Liu, H. Zhang, *Chem. Soc. Rev.* **2015**, *44*, 2584.
[22] C. Zhang, S. Pinilla, N. McEvoy, C. P. Cullen, B. Anasori, E. Long, S.-H. Park, A. Seral-Ascaso, A. Shmeliov, D. Krishnan, C. Morant, X. Liu, G. S. Duesberg, Y. Gogotsi, V. Nicolosi, *Chem. Mater.* **2017**, *29*, 4848.
[23] C. Zhang, S. J. Kim, M. Ghidiu, M.-Q. Zhao, M. W. Barsoum, V. Nicolosi, Y. Gogotsi, *Adv. Funct. Mater.* **2016**, *26*, 4143.
[24] X. Meng, K. He, D. Su, X. Zhang, C. Sun, Y. Ren, H.-H. Wang, W. Weng, L. Trahey, C. P. Canlas, J. W. Elam, *Adv. Funct. Mater.* **2014**, *24*, 5435.
[25] C. Wu, J. Maier, Y. Yu, *Adv. Mater.* **2016**, *28*, 174.
[26] Q. Zhang, S. Tan, R. G. Mendes, Z. Sun, Y. Chen, X. Kong, Y. Xue, M. H. Rümmeli, X. Wu, S. Chen, L. Fu, *Adv. Mater.* **2016**, *28*, 2616.
[27] J. Xiao, D. Choi, L. Cosimbescu, P. Koech, J. Liu, J. P. Lemmon, *Chem. Mater.* **2010**, *22*, 4522.
[28] H. S. S. R. Matte, A. Gomathi, A. K. Manna, D. J. Late, R. Datta, S. K. Pati, C. N. R. Rao, *Angew. Chem. Int. Ed.* **2010**, *49*, 4059.
[29] D. Chen, G. Ji, B. Ding, Y. Ma, B. Qu, W. Chen, J. Y. Lee, *Ind. Eng. Chem. Res.* **2014**, *53*, 17901.
[30] C. Zhang, X. Liu, V. Nicolosi, *Bioenerg.: Open Access* **2016**, *5*, 1.
[31] A. O'Neill, U. Khan, J. N. Coleman, *Chem. Mater.* **2012**, *24*, 2414.
[32] R. J. Smith, P. J. King, M. Lotya, C. Wirtz, U. Khan, S. De, A. O'Neill, G. S. Duesberg, J. C. Grunlan, G. Moriarty, J. Chen, J. Wang, A. I. Minett, V. Nicolosi, J. N. Coleman, *Adv. Mater.* **2011**, *23*, 3944.
[33] V. Nicolosi, M. Chhowalla, M. G. Kanatzidis, M. S. Strano, J. N. Coleman, *Science* **2013**, *340*, 1226419.
[34] Y. Lu, X. Yao, J. Yin, G. Peng, P. Cui, X. Xu, *RSC Adv.* **2015**, *5*, 7938.
[35] K. Chang, W. Chen, *ACS Nano* **2011**, *5*, 4720.
[36] Y. Liu, X. He, D. Hanlon, A. Harvey, J. N. Coleman, Y. Li, *ACS Nano* **2016**, *10*, 8821.

[37] T. Fujita, Y. Ito, Y. Tan, H. Yamaguchi, D. Hojo, A. Hirata, D. Voiry, M. Chhowalla, M. Chen, *Nanoscale* **2014**, *6*, 12458.
[38] X. Xiao, C. Zhang, S. Lin, L. Huang, Z. Hu, Y. Cheng, T. Li, W. Qiao, D. Long, Y. Huang, L. Mai, Y. Gogotsi, J. Zhou, *Energy Storage Mater.* **2015**, *1*, 1.
[39] X. Xiao, Z. Peng, C. Chen, C. Zhang, M. Beidaghi, Z. Yang, N. Wu, Y. Huang, L. Miao, Y. Gogotsi, J. Zhou, *Nano Energy* **2014**, *9*, 355.
[40] N. A. Kumar, M. A. Dar, R. Gul, J.-B. Baek, *Mater. Today* **2015**, *18*, 286.
[41] Y. Liu, X. He, D. Hanlon, A. Harvey, U. Khan, Y. Li, J. N. Coleman, *ACS Nano* **2016**, *10*, 5980.
[42] A. V. Murugan, M. Quintin, M.-H. Delville, G. Campet, C. S. Gopinath, K. Vijayamohanan, *J. Power Sources* **2006**, *156*, 615.
[43] P. Hu, L. Wang, M. Yoon, J. Zhang, W. Feng, X. Wang, Z. Wen, J. C. Idrobo, Y. Miyamoto, D. B. Geohegan, K. Xiao, *Nano Lett.* **2013**, *13*, 1649.
[44] S. Yang, Y. Li, X. Wang, N. Huo, J.-B. Xia, S.-S. Li, J. Li, *Nanoscale* **2014**, *6*, 2582.
[45] Y. Hernandez, V. Nicolosi, M. Lotya, F. M. Blighe, Z. Sun, S. De, I. T. McGovern, B. Holland, M. Byrne, Y. K. Gun'Ko, J. J. Boland, P. Niraj, G. Duesberg, S. Krishnamurthy, R. Goodhue, J. Hutchison, V. Scardaci, A. C. Ferrari, J. N. Coleman, *Nat. Nanotechnol.* **2008**, *3*, 563.
[46] J. N. Coleman, M. Lotya, A. O'Neill, S. D. Bergin, P. J. King, U. Khan, K. Young, A. Gaucher, S. De, R. J. Smith, I. V Shvets, S. K. Arora, G. Stanton, H.-Y. Kim, K. Lee, G. T. Kim, G. S. Duesberg, T. Hallam, J. J. Boland, J. J. Wang, J. F. Donegan, J. C. Grunlan, G. Moriarty, A. Shmeliov, R. J. Nicholls, J. M. Perkins, E. M. Grieveson, K. Theuwissen, D. W. McComb, P. D. Nellist, V. Nicolosi, *Science* **2011**, *331*, 568.
[47] T. M. Higgins, D. McAteer, J. C. M. Coelho, B. Mendoza Sanchez, Z. Gholamvand, G. Moriarty, N. McEvoy, N. C. Berner, G. S. Duesberg, V. Nicolosi, J. N. Coleman, *ACS Nano* **2014**, *8*, 9567.
[48] D. McAteer, Z. Gholamvand, N. McEvoy, A. Harvey, E. O'Malley, G. S. Duesberg, J. N. Coleman, *ACS Nano* **2015**, *10*, 672.
[49] K. Allakhverdiev, J. Hagen, Z. Salaeva, *Phys. Status Solidi* **1997**, *163*, 121.
[50] A. Harvey, C. Backes, Z. Gholamvand, D. Hanlon, D. McAteer, H. C. Nerl, E. McGuire, A. Seral-Ascaso, Q. M. Ramasse, N. McEvoy, S. Winters, N. C. Berner, D. McCloskey, J. F. Donegan, G. S. Duesberg, V. Nicolosi, J. N. Coleman, *Chem. Mater.* **2015**, *27*, 3483.
[51] C. Backes, B. M. Szydłowska, A. Harvey, S. Yuan, V. Vega-Mayoral, B. R. Davies, P.-L. Zhao, D. Hanlon, E. J. G. Santos, M. I. Katsnelson, W. J. Blau, C. Gadermaier, J. N. Coleman, *ACS Nano* **2016**, *10*, 1589.
[52] D. J. Late, B. Liu, H. S. S. R. Matte, C. N. R. Rao, V. P. Dravid, *Adv. Funct. Mater.* **2012**, *22*, 1894.
[53] P. J. King, T. M. Higgins, S. De, N. Nicoloso, J. N. Coleman, *ACS Nano* **2012**, *6*, 1732.
[54] D. Stauffer, A. Aharony, *Computer (Long. Beach. Calif).* **1994**, *1*, 192.
[55] M. S. Dresselhaus, G. Dresselhaus, R. Saito, A. Jorio, *Phys. Rep.* **2005**, *409*, 47.
[56] G. Duesberg, W. Blau, H. Byrne, J. Muster, M. Burghard, S. Roth, *Chem. Phys. Lett.* **1999**, *310*, 8.
[57] N. Nitta, G. Yushin, *Part. Part. Syst. Charact.* **2014**, *31*, 317.
[58] J. Saint, *Solid State Ionics* **2005**, *176*, 189.
[59] H. Senoh, H. Kageyama, T. Takeuchi, K. Nakanishi, T. Ohta, H. Sakaebe, M. Yao, T. Sakai, K. Yasuda, *J. Power Sources* **2011**, *196*, 5631.
[60] V. Augustyn, P. Simon, B. Dunn, *Energy Environ. Sci.* **2014**, *7*, 1597.
[61] V. Augustyn, J. Come, M. Lowe, J. W. Kim, P.-L. Taberna, S. H. Tolbert, H. D. Abruña, P. Simon, B. Dunn, *Nat. Mater.* **2013**, *12*, 518.
[62] C. Zhang, Y. Xie, M. Zhao, A. E. Pentecost, Z. Ling, J. Wang, D. Long, L. Ling, W. Qiao, *ACS Appl. Mater. Interfaces* **2014**, *6*, 9751.
[63] G. A. Muller, J. B. Cook, H.-S. Kim, S. H. Tolbert, B. Dunn, *Nano Lett.* **2015**, *15*, 1911.
[64] Q. Mahmood, S. K. Park, K. D. Kwon, S.-J. Chang, J.-Y. Hong, G. Shen, Y. M. Jung, T. J. Park, S. W. Khang, W. S. Kim, J. Kong, H. S. Park, *Adv. Energy Mater.* **2016**, *6*, 1501115.
[65] S.-H. Bae, K. Karthikeyan, Y.-S. Lee, I.-K. Oh, *Carbon* **2013**, *64*, 527.
[66] J.-Z. Wang, L. Lu, M. Lotya, J. N. Coleman, S.-L. Chou, H.-K. Liu, A. I. Minett, J. Chen, *Adv. Energy Mater.* **2013**, *3*, 798.